

See discussions, stats, and author profiles for this publication at: <https://www.researchgate.net/publication/231645486>

Vertical Stratification and Interfacial Structure in P₃HT:PCBM Organic Solar Cells

ARTICLE in THE JOURNAL OF PHYSICAL CHEMISTRY C · AUGUST 2010

Impact Factor: 4.77 · DOI: 10.1021/jp104695j

CITATIONS

67

READS

64

10 AUTHORS, INCLUDING:



Ben Vaughan

University of Newcastle

12 PUBLICATIONS 157 CITATIONS

SEE PROFILE



Kerry B. Burke

University of Newcastle

16 PUBLICATIONS 353 CITATIONS

SEE PROFILE



Andrew Stapleton

Flinders University

10 PUBLICATIONS 168 CITATIONS

SEE PROFILE



Xiaoqing Zhou

University of Newcastle

58 PUBLICATIONS 404 CITATIONS

SEE PROFILE

Vertical Stratification and Interfacial Structure in P3HT:PCBM Organic Solar Cells

Bofei Xue,^{†,‡} Ben Vaughan,[†] Chung-How Poh,[†] Kerry B. Burke,^{†,‡} Lars Thomsen,[§] Andrew Stapleton,[†] Xiaojing Zhou,[†] Glenn W. Bryant,[†] Warwick Belcher,[†] and Paul C. Dastoor^{*,†}

Centre for Organic Electronics, University of Newcastle, Callaghan, NSW, 2308, Australia, CSIRO Energy Technology, P.O. Box 330, Newcastle, 2300, Australia, and Australian Synchrotron Company Ltd., Clayton, Vic 3168, Australia

Received: May 21, 2010; Revised Manuscript Received: August 9, 2010

Structure and morphology play a critical role in determining the performance of organic photovoltaic devices. In this paper, variation of the postannealing cooling rate is used to create a series of “snapshots” of the vertical and interfacial reorganization processes that occur upon annealing. The data show that slower cooling rates result in significantly enhanced device efficiencies primarily driven by increased short circuit current and fill factor. UV–vis spectroscopy, X-ray diffraction (XRD), near-edge X-ray absorption fine structure spectroscopy (NEXAFS), atomic force microscopy (AFM), and contact angle measurements are used to probe the origin of these improvements. Our results show evidence for a distinct and changing vertical stratification and interfacial structure in the device throughout the annealing process, with both composition and crystallinity varying through the active layer. The implications of these changes are discussed in terms of device properties.

1. Introduction

Organic photovoltaic (OPV) devices are an extremely promising technology for low cost sustainable energy generation.^{1,2} The key feature of these devices is that they can be fabricated over large areas via simple fabrication procedures as flexible plastic films.^{3,4} As a consequence, there have been an increasing number of investigations into the properties and characteristics of OPV devices with a view to improving their power conversion efficiency.^{5–7}

Work over the past decade has shown that the structure and morphology of the active layer are critical parameters in determining the performance of OPV devices.¹ Devices fabricated from 1:1 blends of poly(3-hexylthiophene) (P3HT) and [6,6]-phenyl-C61-butyric acid methyl ester (PCBM) are among the best performing OPV devices with reported power conversion efficiencies of around 4–6%.^{8,9} The effect of annealing upon the active layer of these devices is significant, with device efficiency dramatically increasing after annealing.^{10,11} More recently, devices utilizing modified polythiophene derivatives have led to device efficiencies in excess of 7.4%.¹² The effects of annealing studied on P3HT devices should also be of general use to these and other related polythiophene-based devices.

The origin of the improvement upon annealing has been the subject of much investigation over the past few years. Erb et al. showed that the effect of annealing was primarily to improve the degree of P3HT crystallinity.¹¹ Mihailetchi et al. argued that the addition of PCBM disrupts the hole mobility in P3HT:PCBM blends and that thermal annealing acts to enhance both hole and electron mobility in the devices.¹³ Clarke et al. used transient absorption spectroscopy to demonstrate that thermal annealing results in an approximate 2-fold increase in the yield of dissociated charges and that the enhanced charge generation is

correlated with a decrease in the ionization potential of P3HT.¹⁴ Previous investigations of the effect of annealing upon the morphology of the active layer have shown that heating the film drives the phase segregation of the two components.¹⁵ Prolonged thermal annealing produces ordered P3HT structures and greater than micrometer-sized PCBM crystallites.^{16,17} Although previous investigations have focused on optimizing the duration and temperature of the annealing stage, surprisingly little attention has been paid to the role of cooling rate upon device structure and performance.¹⁷

It is increasingly recognized that vertical phase segregation and structure within OPV devices is at least as important as the lateral phase segregation, the latter of which has received much more attention to date.^{18,19} Over the past few years, there have been several reports on the vertical segregation of semiconducting polymer–fullerene blend systems.^{20–24} In the case of P3HT:PCBM devices, despite a number of publications inferring vertical phase segregation,^{10,25–27} it is only very recently that direct measurements of the vertical composition and structure within the active layer have been reported.^{17,28–38} *However, given the contrasting reports from the literature, a clear picture of the vertical composition and structure of the active layer in these devices is still under debate.*

The variation of vertical composition will clearly play a critical role in all aspects of the charge generation and extraction processes and, as is the case for lateral phase segregation, will heavily influence dissociation and recombination dynamics.^{39–42} Furthermore, interfacial composition will have a major influence on charge transport across the active layer/electrode interfaces. Here, we report the effect of thermal annealing upon the vertical structure and morphology of the active layer. In particular, a combination of UV–vis spectroscopy, X-ray diffraction (XRD), and near-edge X-ray absorption fine structure spectroscopy (NEXAFS) has been used to probe the active layer/air and active layer/substrate interfaces. A particular focus was the effect of the postannealing cooling rate upon the vertical structure of the device and device performance. The results show that the

* To whom correspondence should be addressed. E-mail: Paul.Dastoor@newcastle.edu.au.

[†] University of Newcastle.

[‡] CSIRO Energy Technology.

[§] Australian Synchrotron Company Ltd.

interfacial structure of P3HT:PCBM blends is more complex than previously thought with aligned capping and wetting layers present at the active layer/air and active layer/substrate interfaces, respectively. The cooling rate has a significant effect on the active layer structure with increased polymer interchain and interfacial order observed for the slowest cooled devices, consistent with their improved photovoltaic performance.

2. Experimental Section

2.1. Device Fabrication. PEDOT:PSS (Baytron P) films were spin-coated (5000 rpm) on precleaned patterned ITO glass slides and annealed at 120 °C for 30 min to eliminate water in the films. The PEDOT:PSS films were transferred into a glovebox with a dry nitrogen atmosphere to prevent humidity uptake. A weight ratio of 1:1 was used for all P3HT (Rieke Metal) and PCBM (Solenne B.V.) blends. The P3HT:PCBM blend solution (25 mg/mL in chloroform) was sonicated for 30 min and then used to spin-coat the active layers in an inert atmosphere glovebox at 2000 rpm for 1 min. These active layers were then transferred into a vacuum chamber for electrode evaporation. The calcium (Ca) electrodes were evaporated on the active layers in a vacuum (2×10^{-6} Torr). Aluminum (Al) layers were then evaporated on top of the Ca layers. The thickness of Ca and Al layers was measured to be about 20 and 70 nm, respectively, by a KLA Tencor profilometer, and the area of each cell was 4 mm². After the evaporation, fabricated devices were annealed at 140 °C on a hot plate (temperature variation ± 2 °C) for 4 min. For fast cooling and medium cooling, after annealing, the samples were placed on a metal substrate and a piece of thick paper, respectively. For slow cooling, the hot plate was turned off and the sample was left on the hot plate until the temperature reached room temperature. For different cooling rates, the temperature of the glass slides was measured by a type K thermocouple. The variation of substrate surface temperature as a function of time for the three different cooling rates was fitted using Newton's law of cooling to extract the cooling rate, k (see the Supporting Information). The three cooling rates were chosen to be reasonably evenly distributed, and the cooling rate values are tabulated in Table 2.

2.2. Device Characterization. For the UV-vis and XRD characterization, the relevant films were spin coated on normal silica glass slides following procedures mentioned above. An ultraviolet-visible absorption spectrophotometer (UV-vis, Varian Cary 6000i) was used to study the absorption of P3HT-PCBM blend films (unannealed and annealed, with different cooling rates) and also pure P3HT films (unannealed and annealed, medium cooled) as a reference. A Philips X'Pert MPD X-ray diffractometer (Ni-filtered Cu K α radiation) was used to investigate the crystallinity of the active layers. The morphology of P3HT-PCBM films was observed by a Digital Instruments NanoScope IIIa Multimode atomic force microscope (AFM). The contact angle of a stationary water sessile drop on the P3HT, PCBM, and P3HT:PCBM materials was measured equilibrated in a vapor of water using an OCA20 instrument (DataPhysics Instruments, Germany). For these measurements, the evaporation of the metal electrode was omitted.

The photocurrent density-voltage (J - V) measurements were conducted using a Newport Class A solar simulator with an AM 1.5 spectrum filter to illuminate the full cells. The light intensity was measured to be 90 mW cm⁻² by a silicon reference solar cell (FHG-ISE), and the J - V data were recorded by a Keithley 2400 source meter.

NEXAFS spectra were recorded at angles of 20, 55, and 90°, measured between the direction vector of the incident linear

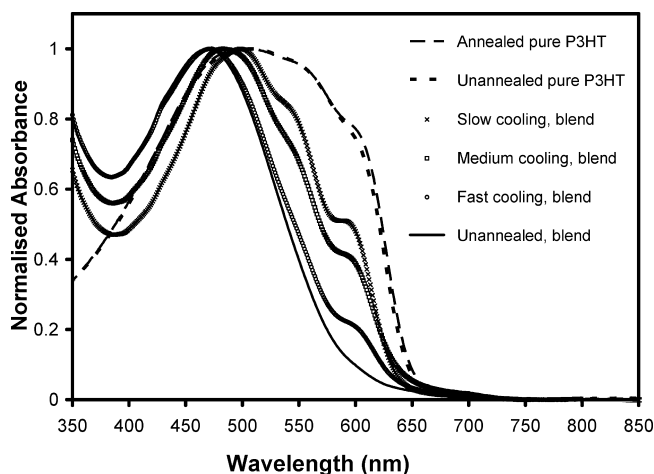


Figure 1. UV-vis spectra of pure P3HT films (unannealed and annealed (medium cooled)) and P3HT:PCBM blend films (unannealed and annealed (slow, medium, and fast cooled)).

polarized light and the surface plane of the sample. Thus, for an angle of 90°, the electric field vector, E , will be parallel to the surface plane, whereas at 20° E will be almost perpendicular to the surface plane. Samples for NEXAFS analysis were prepared with the metal electrodes omitted. The samples for analysis of the active layer/substrate interface were obtained by lifting off the films in deionized water and inverting onto a doped silicon substrate. The samples for analysis of the active layer/air interface were deposited directly onto a doped silicon substrate. Spectra were acquired at the carbon K-edge using both total electron yield (TEY) and Auger electron yield (AEY). The kinetic energy window was selected between 262 and 272 eV to ensure that the detection window encompassed the KVV carbon Auger edge at 264 eV. The raw spectra were normalized as discussed by Watts et al.,⁴³ and the changes in the preferential orientation of the P3HT polymer were elucidated from the normalized C K-edge structure. X-ray beam damage tests were conducted by continuously exposing test samples to the X-ray beam until significant changes in the normalized C K-edge structure occurred. The exposure time of samples to the synchrotron beam was subsequently restricted to less than this critical time. The size of the synchrotron beam is 500 μ m \times 500 μ m, and thus, the NEXAFS spectra presented in this study represent the average orientation of the P3HT chains at the surface of the film.

3. Results and Discussion

3.1. UV-vis Spectra. Figure 1 shows the normalized UV-vis absorbance spectra for the unannealed and annealed P3HT:PCBM blend films, as well as the normalized UV-vis absorbance spectra for the unannealed and annealed pure P3HT films. The film thicknesses of the blend films were 250 nm ($\pm 6\%$), while the absorbance of the pure P3HT films was calculated from the reflection and transmission spectra.

It is well established that the position of the P3HT peak absorbance band (at around 500 nm) provides information on the degree of conjugation of the polymer chains, while the relative size of the P3HT vibronic shoulder (at around 600 nm) provides information on the degree of interchain order.⁴⁴ As such, the combination of these two spectral features provides a simple indication of the extent of local P3HT order. The annealed pure P3HT film exhibits similar conjugation length and interchain order to that of the unannealed pure P3HT film, in agreement with previous observations.^{46,47} Furthermore, the

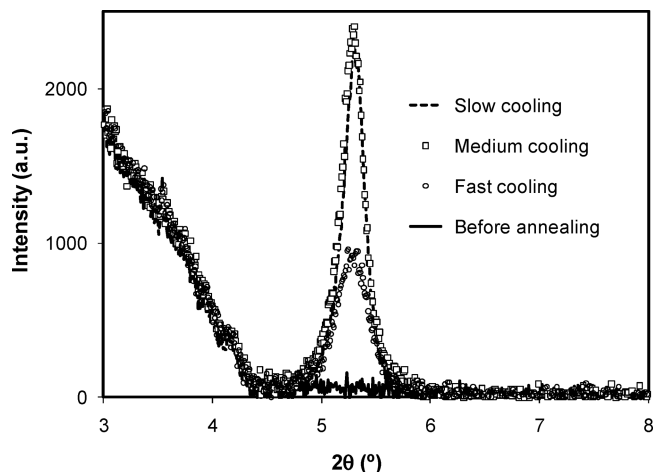


Figure 2. X-ray diffraction spectra of P3HT:PCBM blend films, unannealed and annealed with different cooling rates.

spectra of the annealed pure P3HT films are independent of the cooling rate. In comparison with the blend films, the pure P3HT films exhibit red-shifted absorbance spectra, indicating longer polymer conjugation lengths than that observed in the blend films, consistent with previous observations.^{45–47} For the blend films, both the red-shift of the main absorbance band and the size of the vibronic shoulder increase systematically from the unannealed film through the fast, medium, and slow cooled films, respectively. The unannealed P3HT:PCBM blend films show the shortest P3HT conjugation length and lowest degree of interchain order, both of which are much lower than that observed for the pure P3HT films, indicating that introduction of PCBM into the blend disrupts the local ordering of the polymer. Upon annealing, P3HT conjugation length and interchain order increase and the extent of this increase changes systematically as a function of the postannealing cooling rate, with the slowest cooled films exhibiting the longest conjugation length and the greatest local ordering in the P3HT:PCBM blend films. However, it should be noted that the degree of polymer order never regains the levels observed for the pure P3HT films.

3.2. XRD Spectra. Figure 2 shows the XRD spectra ($3^\circ < 2\theta < 8^\circ$) for the unannealed and annealed P3HT:PCBM blend films prepared using the three different postannealing cooling rates. The XRD spectrum for the unannealed blend film is essentially featureless, whereas the spectra for the annealed film exhibit a peak at $2\theta = 5.3^\circ$ (with an incident X-ray wavelength, $\lambda = 0.154$ nm), which is larger for the medium and slow cooled blend films than for the fast cooled blend. The peaks for medium and slow cooled blend films are almost identical. The peak at 5.3° originates from Bragg reflections from P3HT crystallites with *a*-axis orientation.¹¹ Although not shown here, wide range XRD spectra ($3^\circ < 2\theta < 30^\circ$) were also recorded, but no peaks at higher angles corresponding to the presence of P3HT crystallites with *b*- or *c*-axis orientation ($2\theta \sim 23^\circ$)¹¹ or pure PCBM crystallites ($2\theta \sim 19^\circ, 28^\circ$)^{11,47} could be detected. As such, the XRD data indicates that the PCBM acts to disrupt the preferred *a*-axis crystallinity of the P3HT in the bulk of the blend film. Upon annealing, *a*-axis crystallites are formed with a lower crystallite volume density for the fast cooled sample than for the medium and slow cooled blends.

3.3. NEXAFS Spectra. **3.3.1. General Description.** Whereas XRD probes the bulk crystallinity of the active layer, near edge X-ray absorption fine structure spectroscopy (NEXAFS) can be used to probe the chemical composition and molecular order of surfaces.^{43,48} Furthermore, by utilizing different yield tech-

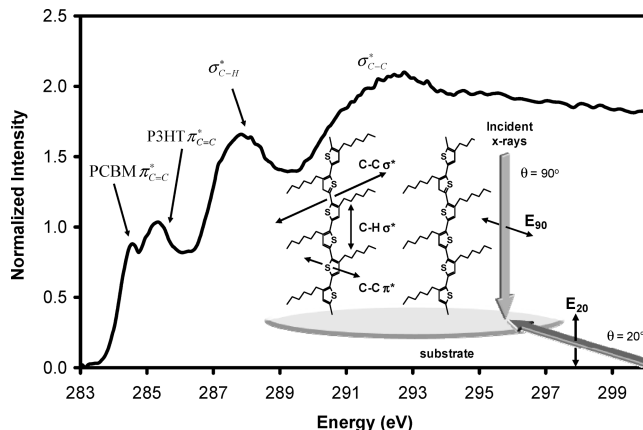


Figure 3. Carbon K-edge NEXAFS spectrum for unannealed P3HT:PCBM at the active layer/air interface showing the assignments for the main transitions. Inset: Schematic diagram of the relative polarization of the P3HT molecular bonds for *c*-axis aligned P3HT molecules and **E** vector of the X-ray beam for different incident angles.

niques, NEXAFS can be used to elucidate the chemical composition by depth at, or near, the film surface. A combination of Auger electron yield (AEY) and total electron yield (TEY) techniques were used to examine the chemical composition at the active layer/air and active layer/substrate interfaces for unannealed and postannealed films.

Angle-resolved NEXAFS is a well-established technique for determining the orientation of organic molecules.⁴⁸ Figure 3 shows the positions of the characteristic molecular transitions in the carbon K-edge spectrum of a P3HT:PCBM blend film. At the lowest energy, there are two C 1s $\rightarrow \pi^*_{C=C}$ transitions corresponding to the PCBM and thiophene ring moieties (~ 285 and 286 eV, respectively) with the polarization of the P3HT $\pi^*_{C=C}$ transition lying normal to the thiophene ring.⁴⁹ Progressing to higher energies (~ 287 – 289 eV), there are peaks corresponding to the σ^*_{C-H} transitions with polarization normal to the alkyl chain. At still higher energy (~ 293 eV), there are overlapping peaks due to σ^*_{C-C} transitions from both components with the P3HT transitions arising from σ^*_{C-C} contributions from the alkyl group and the polymer backbone with polarizations parallel to the C–C chain in both cases. The polarization alignment of these transitions can be probed by comparing NEXAFS spectra recorded across a range of incident angles (Figure 3, inset). For an angle of 90° , the radiation will be at normal incidence and the polarized electric field vector, **E**, will be parallel to the substrate plane and hence transitions whose dipole moments are aligned parallel to the substrate will show the greatest resonance signal in the NEXAFS spectrum. However, at 20° , the incident radiation is at a glancing angle and **E** is almost perpendicular to the surface plane and thus the largest NEXAFS signals will arise from bonds whose dipole moments are normal to the surface.

3.3.2. NEXAFS of Substrate/Active Layer Interface. Figure 4 shows the carbon K-edge TEY NEXAFS spectra collected with the X-ray beam at angles of $20, 55$, and 90° to the surface of the active layer/substrate interface for unannealed (Figure 4a) and postannealed P3HT:PCBM films that were slow cooled (Figure 4b) and fast cooled (Figure 4c). For the unannealed film, the absorption at ~ 285 eV (peak I) exhibits a lower energy shoulder and main peak at all incidence angles. As can be seen from the expanded view of peak I (Figure 5), this peak consists of contributions from PCBM, P3HT, and PEDOT:PSS. Despite extensive washing, it is clear that PEDOT:PSS is still present at this interface, indicating that either the P3HT and PEDOT:

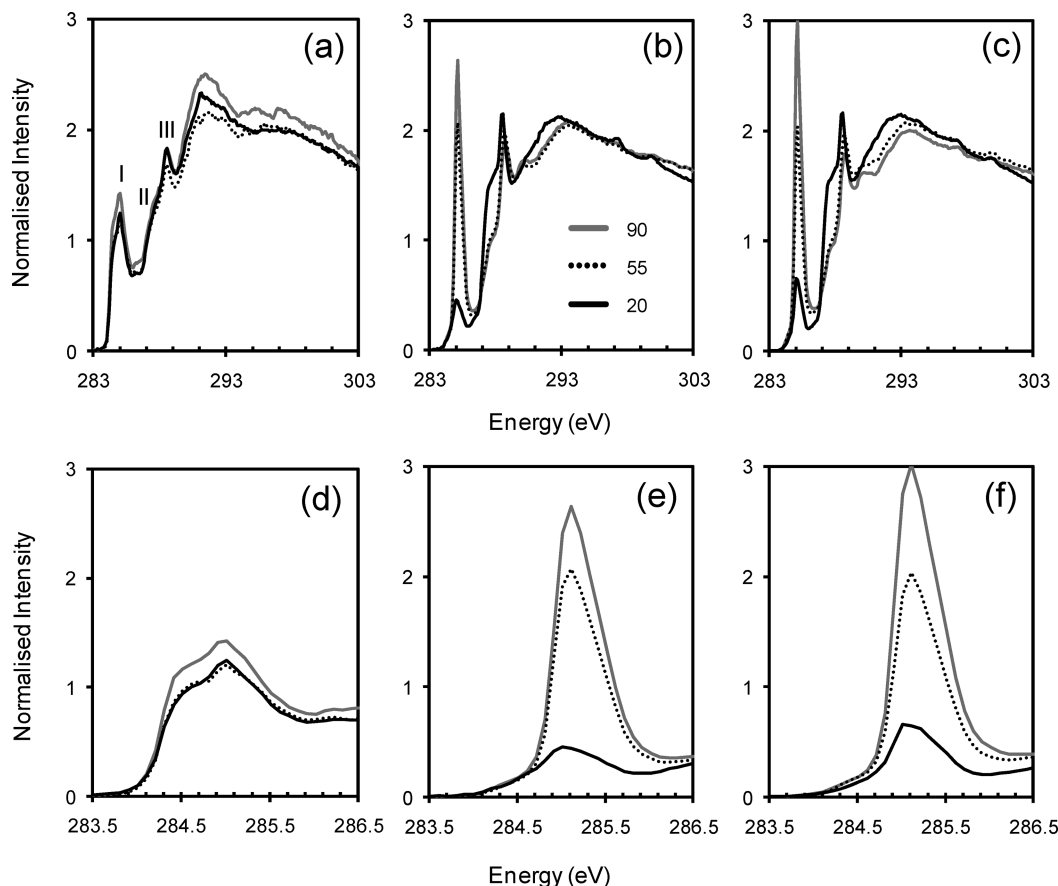


Figure 4. Carbon K-edge TEY NEXAFS spectra (20, 55, and 90° incidence) of the active layer/substrate interface for unannealed and postannealed P3HT:PCBM blend films with different cooling rates: (a) unannealed, (b) slow cooled, (c) fast cooled. Expanded views of peak I for unannealed and postannealed P3HT:PCBM blend films with different cooling rates: (d) unannealed, (e) slow cooled, (f) fast cooled.

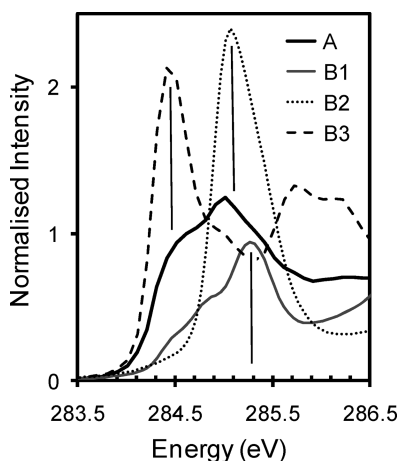


Figure 5. Carbon K-edge TEY NEXAFS spectra (20° incidence) of the active layer/substrate interface for an unannealed P3HT:PCBM film (A: solid black line), together with the carbon K-edge TEY spectra (20° incidence) for pure P3HT (B1: solid gray line), PEDOT:PSS (B2: dotted line) and PCBM (B3: dashed line) films. All of the pure films were unannealed and only the $\pi^*_{C=C}$ region of the NEXAFS spectra is shown. The data shows that the P3HT:PCBM signal contains components associated with the P3HT, PEDOT, and PCBM spectra.

PSS layers are intermixed or that there is a thin intractable PEDOT:PSS film overlaying the P3HT. The presence of irremovable PEDOT:PSS at this interface is consistent with the findings of other groups who also observed a PEDOT:PSS residue upon delamination.^{34,38,50,51} The lack of dichroism in Figure 4a indicates that there is no alignment of the components in the unannealed film.

Upon annealing, two main changes to the NEXAFS spectra are observed for both the slow cooled and fast cooled samples. First, the lower energy shoulder due to the PCBM $\pi^*_{C=C}$ transition is no longer present. Thus, within the depth sensitivity of TEY (~ 3 nm),⁵² it would appear that upon annealing the PCBM diffuses into the bulk of the film and is no longer present at the substrate interface.

Second, the loss of PCBM at the interface coincides with a dramatic increase in the dichroism of the peak at 285.1 eV. Given that the interfacial layer contains both PEDOT:PSS and P3HT, this observed dichroism could originate from either of the components or from a mixture of the two. One possibility is that the observed dichroism arises solely from the remnant PEDOT:PSS at the active layer/substrate interface. Indeed, Aasmundtveit et al. showed that PEDOT doped with small tosylate counterions formed aligned films upon annealing.⁵³ However, Casu et al. have demonstrated that NEXAFS measurements on annealed PEDOT:PSS films exhibit no dichroism.⁵⁴ It is well established that PEDOT:PSS forms spherical grains (of average diameter 50–80 nm) consisting of tangles of PEDOT segments adhering to single PSS chains.⁵⁵ The structures consist of a hydrophobic PEDOT-rich core surrounded by a PSS-rich shell with no overall alignment of the PEDOT segments within grains. Furthermore, STM studies by Nardes et al. showed that annealed PEDOT:PSS films consist of randomly oriented submicrometer sized domains which would not produce the observed dichroism in the NEXAFS measurement.⁵⁶ As such, it seems unlikely that alignment occurring at this interface is due to PEDOT:PSS. We therefore believe that the dichroism observed in the NEXAFS signal arises from the

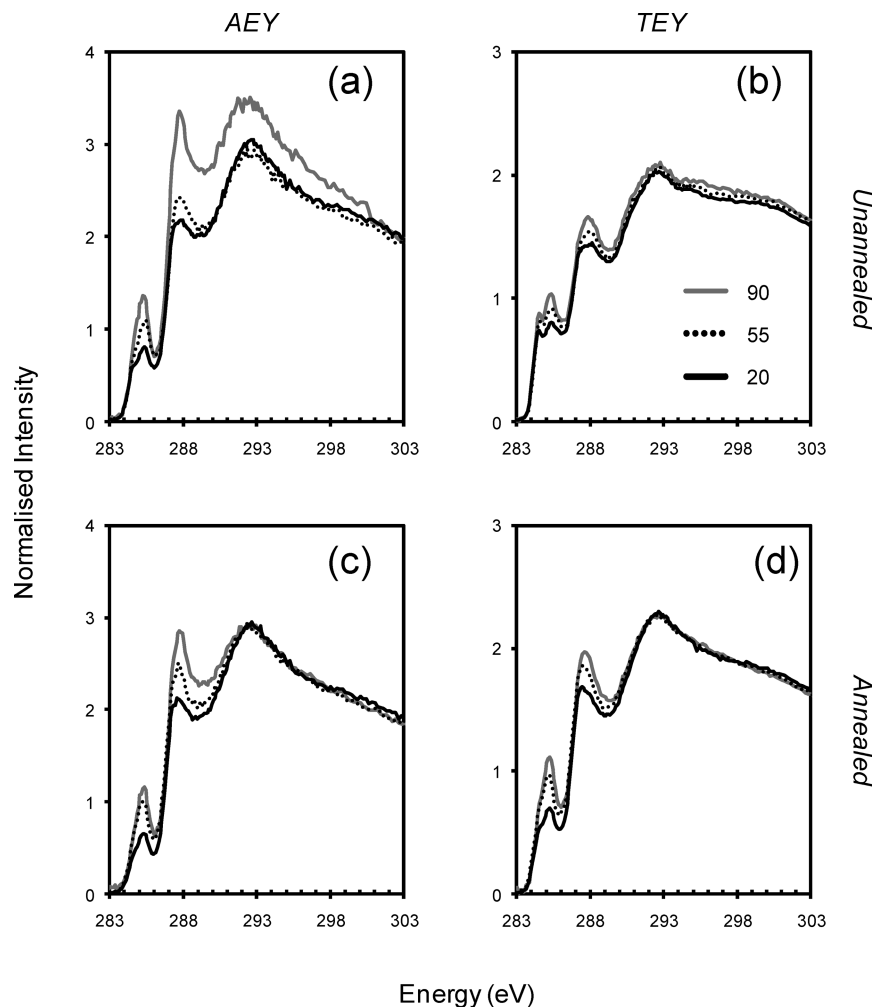


Figure 6. Carbon K-edge AEY and TEY NEXAFS spectra (20, 55, and 90° incidence) of the active layer/air interface for annealed and postannealed P3HT:PCBM films: (a) unannealed AEY, (b) unannealed TEY, (c) annealed AEY, (d) annealed TEY.

alignment of the P3HT component at the interface. This view is further supported by the observation that the peak structure at 288.5 eV (peak III), which is primarily associated with the PEDOT absorption spectrum, shows little variation with incident angle, whereas the shoulder at 287.4 eV (peak II), which is primarily associated with the P3HT absorption spectrum, and the peak at 285.1 eV both show a strong dichroic response. Thus, our interpretation of the data is that, while the annealed NEXAFS spectra exhibit characteristics of both PEDOT and P3HT, the observed dichroism arises from the P3HT component.

On the basis of this interpretation, a comparison of the three panels in Figure 4 reveals that, whereas the unannealed film is effectively unaligned, the postannealed films exhibit a strong enhancement of the P3HT $\pi^*_{C=C}$ peak at 90° incidence, indicating that the thiophene rings are normal to the interface, which is consistent with either an *a*-axis or *c*-axis oriented structure.¹¹ In addition, the annealed fast cooled and slow cooled NEXAFS spectra show alignment of the P3HT σ^*_{C-H} peak at 287.4 eV (peak II) with the resonance maximized at 20° incidence. This dipole alignment is consistent with the alkyl chains being parallel with the interface in either a *b*-axis or *c*-axis oriented structure. Combining these two observations allows us to conclude that after annealing there exists *c*-axis aligned P3HT at the substrate interface. These NEXAFS observations indicate that, once again, the presence of PCBM in the blend film acts to disrupt the preferred crystallinity of the P3HT at the active layer/substrate interface, consistent with the previous XRD measurements. The

relative alignment of the two annealed samples can be gauged by the ratio of the P3HT $\pi^*_{C=C}$ peak at 90° incidence to that at 20° incidence. Although the magnitude of the $^{90}\pi^*_{C=C}$ peak is smaller for the slow cooled sample, the $^{90}\pi^*_{C=C}:^{20}\pi^*_{C=C}$ ratio is larger at 5.94 in comparison with a value of 4.67 for the fast cooled sample. Thus, the extent of alignment of the slow cooled layer is higher than that of the fast cooled layer.

3.3.3. NEXAFS of Active Layer/Air Interface. Figure 6 shows the carbon K-edge AEY and TEY NEXAFS spectra collected with the X-ray beam at angles of 20, 55, and 90° to the surface of the active layer/air interface for unannealed (Figure 6a and b) and postannealed P3HT:PCBM films that were medium cooled (Figure 6c and d), respectively. Comparing Figure 6a and b, it would appear that, for the unannealed film, the PCBM and P3HT $\pi^*_{C=C}$ transitions at ~285 eV are both strongly present in the TEY NEXAFS spectrum but that the relative contribution from PCBM is less in the AEY NEXAFS spectrum. Since AEY has a depth sensitivity of only ~1.5 nm,⁵² these observations indicate that even for the unannealed sample there is evidence for enhanced P3HT concentration at the air interface. Upon annealing, the PCBM $\pi^*_{C=C}$ shoulder becomes less significant in both the AEY and TEY spectra. Thus, upon annealing, PCBM diffuses into the bulk of the blend structure.

In terms of P3HT alignment, we observe that all of the NEXAFS spectra exhibit an enhancement of the P3HT $\pi^*_{C=C}$ at 90° incidence (similar to the situation at the substrate interface), indicating that the thiophene rings are normal to the air interface,

TABLE 1: Aqueous Contact Angle Measurements of the Active Layer/Air Interface for Pure P3HT Films, Pure PCBM Films, and P3HT:PCBM Blend Films

film materials	contact angle (deg)			
	unannealed	annealed, fast cooled	annealed, medium cooled	annealed, slow cooled
pure P3HT	101.9		102.1	
pure PCBM	50.0		75.4	
P3HT:PCBM	102.0	104.0	105.5	106.0

The measurement errors are better than $\pm 2.5\%$ for all of the material surfaces except for the unannealed pure PCBM surface which had a measurement error of $\pm 15\%$ due to limited delamination of the unannealed PCBM film.

which is consistent with either an *a*-axis or *c*-axis oriented structure. However, now the alignment of the σ_{C}^* peaks is also maximized at 90° incidence. This dipole alignment is consistent with the alkyl chains being normal to the air interface, and thus, the dominant alignment must be the *a*-axis oriented structure. In addition, the differences between the P3HT alignment in the unannealed and annealed samples are more subtle than those observed in Figure 4. For the unannealed film, the AEY spectra show a greater degree of P3HT alignment than

the TEY spectra, which is again consistent with the increased PCBM content in the TEY spectra. Thus, it would appear that there is a higher concentration of more highly aligned P3HT in the upper 1.5 nm of the unannealed P3HT:PCBM blend film. Upon annealing, the thickness of this outermost aligned surface layer increases to at least 3 nm (since the AEY and TEY spectra become much more similar) driven by the diffusion of PCBM into the bulk of the blend film. These observations are consistent with the lower surface energy of P3HT (26.9 mN m^{-1})⁵⁷ compared with PCBM (38.2 mN m^{-1}),²⁴ which will tend to drive P3HT to the outermost surface upon annealing and form a capping layer at the active layer/air interface.

3.4. Contact Angle Measurement. Further evidence for the presence of a P3HT capping layer at the active layer/air interface is obtained from a comparison of the aqueous contact angle measurements for unannealed and postannealed P3HT:PCBM blend films with those of the pure P3HT and pure PCBM films. Table 1 reveals that the aqueous contact angles (and hence surface energy) of the unannealed and postannealed medium cooled P3HT:PCBM blend films are very close to that of a pure P3HT film, as opposed to the much lower contact angle value of a pure PCBM film. Slow and fast cooled P3HT:PCBM blend films have contact angles of 106 and 104° , respectively (Table 1). As such, these measurements support the conclusion that

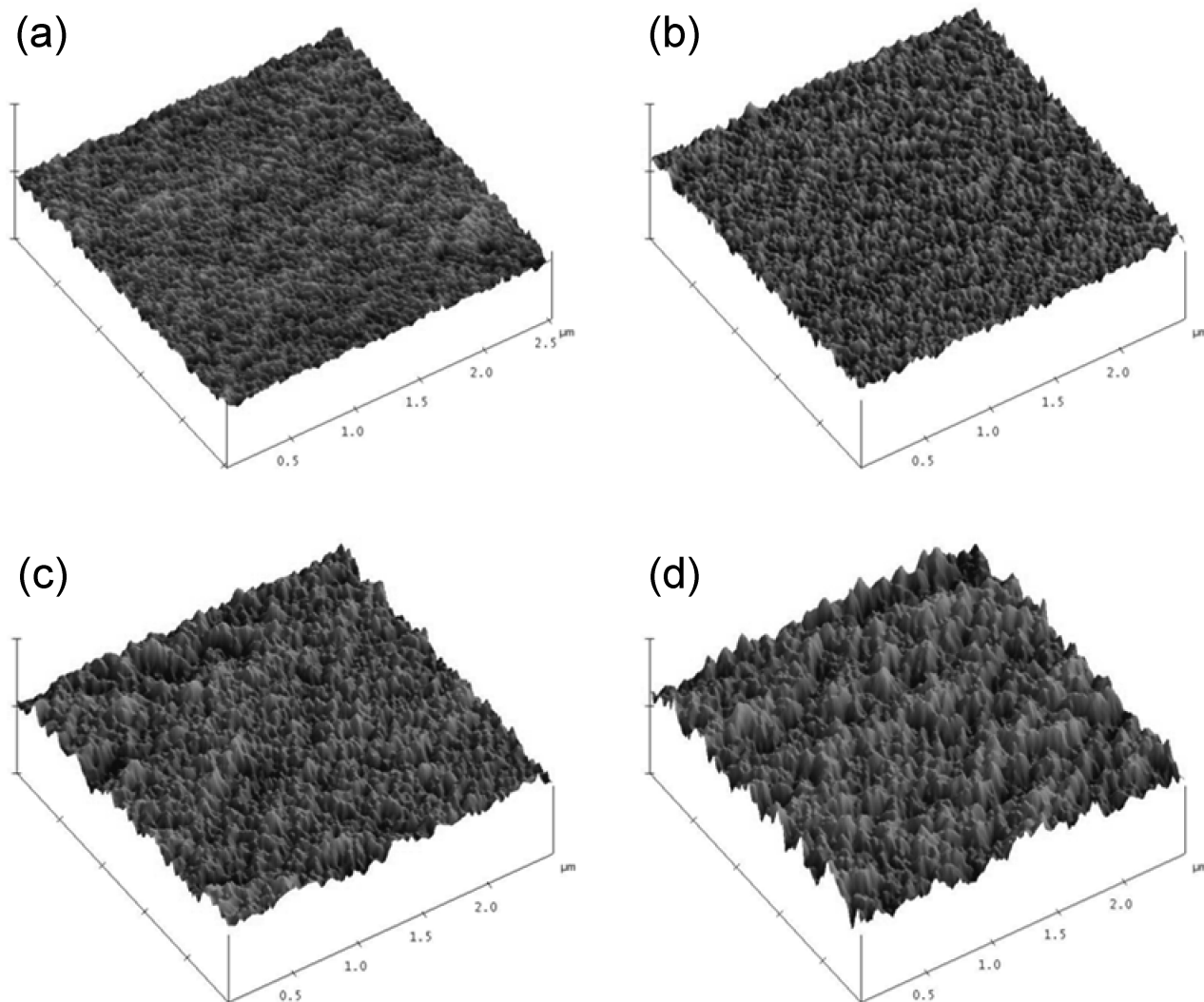


Figure 7. AFM images of unannealed and postannealed P3HT-PCBM films cooled at different rates: (a) unannealed, (b) fast cooled, (c) medium cooled, (d) slow cooled. The vertical and horizontal data scales are 5 nm and $2.5 \times 2.5 \mu\text{m}$, respectively.

TABLE 2: Cooling Rates and Surface Roughness for Unannealed and Post-Annealed P3HT:PCBM Films Cooled at the Three Different Rates^a

sample	k (s ⁻¹)	R_{rms} (nm)	J_{sc} (mA/cm ²)	V_{oc} (V)	FF (%)	PCE (%)	R_s (Ω cm ²)	R_p (Ω cm ²)
unannealed		0.46	3.84	0.612	38.2	1.00	82.9	185.6
fast cooling	0.118	0.68	7.09	0.635	30.1	1.51	137.2	71.6
medium cooling	0.050	1.22	8.21	0.613	45.0	2.51	23.1	115.0
slow cooling	0.001	1.73	9.09	0.597	55.0	3.32	7.0	192.6

^a Device characteristics of OPV cells made from these films are also shown. The surface roughness values were taken from AFM images collected for active layers fabricated with no metal top electrodes.

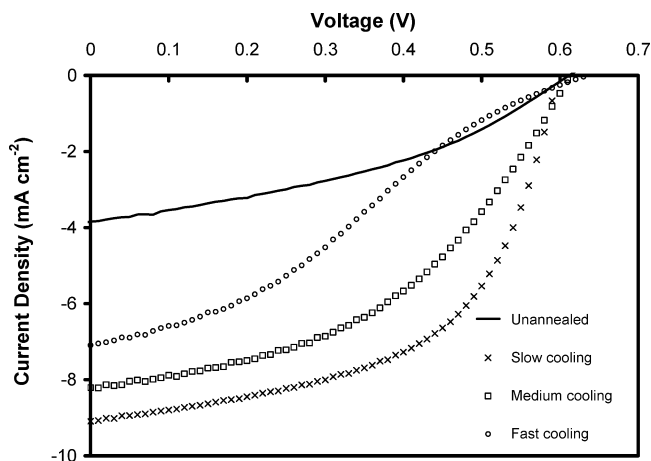


Figure 8. Current density–voltage (J – V) characteristics of OPV cells made from P3HT:PCBM blend films, unannealed and annealed with different cooling rates.

there is a P3HT capping layer present on both the unannealed and annealed blend surfaces.

3.5. Atomic Force Microscopy (AFM) Images. AFM was used to probe the morphology of the active layer/air interface of the unannealed film and the postannealed films cooled at the three different cooling rates. The AFM images (Figure 7) reveal that the unannealed film is significantly smoother than the annealed films and that the surface roughness increases systematically from the fast to slow cooled samples (Table 2).

It is well established that the P3HT and PCBM in the unannealed films are intimately mixed (and hence relatively smooth) and upon annealing phase segregation occurs, resulting in a surface roughening of the blend films, which is characteristic of high efficiency P3HT:PCBM solar cells.⁵⁸ Slower cooling rates allow more time for component diffusion and rearrangement in the active layer of the films, resulting in rougher surfaces. Indeed, the observed trend in surface roughness with cooling rate is broadly consistent with previous work on solvent annealing of films, which also showed that allowing P3HT:PCBM films to evolve for a longer time in a high vapor pressure solvent atmosphere resulted in coarsening of the films.⁵⁹

3.6. J – V Characteristics of Solar Cells. Figure 8 shows the current density–voltage (J – V) characteristics of OPV cells made from P3HT:PCBM blend films, unannealed and annealed with different cooling rates, with the key device parameters listed in Table 2. It is clear that device efficiency is improved upon annealing as expected and that the improvement varies systematically with cooling rate, with the slowest cooled devices exhibiting the highest efficiencies. This trend in device efficiency is correlated with a similarly systematic increase in the short circuit current density (J_{sc}) with decreasing cooling rate. These changes in device performance cannot solely be due to increasing polymer crystallinity, since the XRD data (Figure 2) shows that there is effectively no change in bulk crystallinity of the medium and slow cooled devices. Moreover, the series resistance

(R_s), parallel resistance (R_p), and fill factor (FF) device parameters are all worst for the fast cooled device, indicating that there are competing effects determining the overall performance of the devices.

3.7. Influence of Cooling Rate. Recent studies have shown that different fabrication protocols (such as thermal annealing, vapor annealing, and rate of solvent drying) all lead to common active layer morphologies and device characteristics.³³ As such, altering the postannealing cooling rate simply varies the time available for the P3HT and PCBM components to diffuse and reorder before the system is quenched and the final structure is “frozen in”. The devices investigated here therefore present a series of snapshots of the reorganization process, with the fast cooled sample being furthest from equilibrium and the slow cooled device being closest to the final reorganized state. On the basis of the preceding discussion, the vertical structure of the devices is considerably more complex than previously thought^{17,28–38} and consists of at least three distinct vertically stratified layers: (a) a P3HT-rich substrate interfacial (wetting) layer, (b) a bulk film layer, and (c) a P3HT-rich air interfacial (capping) layer.

Upon spin coating and prior to annealing, the blend film forms a thin polymer-rich layer at the air interface, with the polymer exhibiting some degree of a -axis alignment. At this stage, both the bulk and substrate layers are effectively disordered and probably indistinct. The more surface sensitive nature of the NEXAFS technique means that we are able to detect the presence of a distinct P3HT-rich capping layer, whereas previous ellipsometry data suggests that the interfacial P3HT:PCBM ratio should be closer to 50:50.³³ The observation of a P3HT capping layer is supported by our surface contact angle measurements and by the XPS measurements of Xu et al.³⁴ Furthermore, our NEXAFS results indicate that, in the absence of metal electrodes, the thickness of this capping layer increases upon annealing.

Upon annealing, a distinct polymer-rich wetting layer that exhibits strong c -axis alignment is formed. The formation of a P3HT-rich wetting layer is consistent with recent studies using ellipsometry,³³ TEM tomography,²⁸ and confocal microscopy²⁹ but disagrees with the X-ray photoelectron spectroscopy (XPS) study of Xu et al. who suggested that the PCBM concentration is enhanced at the substrate interface and changes little upon annealing.³⁴ From our fast cooling results, it is clear that the formation of this wetting layer occurs early on in the reorganization process with PCBM diffusing rapidly into the bulk.

In contrast, the ordering of the P3HT chains in the bulk layer occurs over a long time scale, with the XRD and UV–vis data showing that the fast cooled device is only partially ordered both in terms of interchain order and bulk crystallinity. This observation is consistent with the device data, with the fast cooling J – V curve exhibiting an inflection characteristic of reduced dissociation efficiency of bound electron–hole pairs.⁶⁰ Intuitively, one might expect that this reduced dissociation would result in an increased recombination rate and hence a lower V_{oc} .⁶¹ However, in this case, V_{oc} is actually maximized for the fast

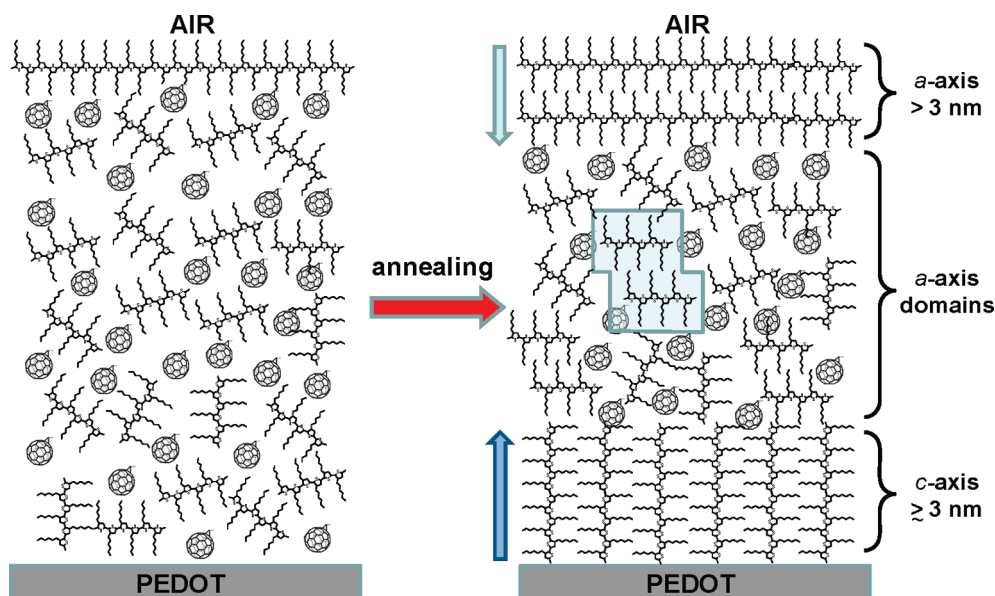


Figure 9. Schematic representation of the vertical stratification that occurs upon annealing P3HT:PCBM blend films. Vertical arrows indicate the growth of aligned P3HT-rich capping and wetting layers upon annealing. The shaded box highlights the development of *a*-axis aligned P3HT domains in the bulk of the active layer following annealing.

cooled device and thus, as observed in other polymer systems,⁶¹ dissociation and recombination are not correlated, which is, we expect, indicative of a complex quenched morphology.⁶⁰

The next stage in the ordering process, as shown by the medium cooling results, involves the polymer crystallinity of the bulk layer and the thickness and order of the polymer-rich capping layer increasing. At the same time, the P3HT interchain order in the blend film is also improved.

Finally, the slow cooling results show that the last stages in the reorganization process involve a progressive increase in the *c*-axis alignment of the wetting layer and further interchain ordering of the polymer. In addition, PCBM diffusion continues and results in an ongoing roughening of the surface. The outcome of these processes is summarized in Figure 9, which shows a schematic representation of the vertical stratification that occurs upon annealing P3HT:PCBM blend devices.⁶²

The data presented here demonstrates that thermal annealing results in the creation of a P3HT-rich layer at both the critical device interfaces. The presence of an enhanced concentration of aligned donor (P3HT) at the substrate interface is likely to be beneficial for device performance by enhancing charge transport to the ITO electrode. On the other hand, the presence of a thin donor-rich capping layer in an OPV device could be detrimental to device performance, since such a layer is likely to act as a site for charge recombination. However, in an aluminum electrode capped device, it is known that thermal diffusion of aluminum into the organic layer occurs during annealing and that this interlayer region may be as thick as 17 nm.⁶³ Thus, at the cathode, device annealing appears to involve a complex balance between the diffusion of PCBM into the bulk of the film, to create a thicker donor capping layer, and diffusion of aluminum through the capping layer into the bulk film to allow effective charge transport. Nonetheless, it is possible to speculate that the presence of a P3HT capping layer must still result in recombination losses within the device and thus the elimination of this layer offers an opportunity for device improvement.

4. Conclusions

Variation of the postannealing cooling rate has been used to create a series of “snapshots” of the reorganization processes

that occur upon annealing. P3HT:PCBM blend devices exhibit a complex vertical stratification of both crystallinity and blend composition. Using a combination of UV-vis spectroscopy, XRD, NEXAFS, AFM, and contact angle measurements, we have shown that annealing results in the formation of three distinct vertical layers. Diffusion of PCBM from the interfaces into the bulk blend film results in the formation of (a) a P3HT-rich substrate interfacial (wetting) layer, (b) a blended bulk film layer, and (c) a P3HT-rich air interfacial (capping) layer. The orientation of the P3HT molecules varies from a wetting layer of *c*-axis aligned P3HT at the substrate interface to an *a*-axis aligned P3HT capping layer at the air interface with an intervening bulk layer that shows *a*-axis alignment. The data show that by slowing the postanneal cooling rate devices with significantly enhanced efficiencies can be prepared. This improvement in device performance is correlated with the observed increased crystallinity, polymer alignment, and phase segregation both at the interfaces and in the bulk film. In particular, slow cooling results in an aligned interfacial active layer/substrate structure that is beneficial for charge transport.

Acknowledgment. The authors acknowledge the financial support from the Australian Synchrotron Research Program. The NEXAFS measurements were undertaken on the soft x-ray spectroscopy beamline at the Australian Synchrotron, Victoria, Australia, and on beamline BL24A1 at the National Synchrotron Radiation Research Center (NSRRC), Hsinchu, Taiwan. The authors gratefully acknowledge the help and assistance of Dr Bruce Cowie and Dr Anton Tadich of the Australian Synchrotron and Dr Yaw-Wen Yang and Dr Liang-Jen Fan of the NSRRC. The authors gratefully acknowledge the help and assistance of Ms. Jenny Zobec in University of Newcastle for XRD measurements.

Supporting Information Available: Variation of temperatures for different cooling rates and the calculation of cooling rates. This material is available free of charge via the Internet at <http://pubs.acs.org>.

References and Notes

- (1) Günes, S.; Neugebauer, H.; Sariciftci, N. S. *Chem. Rev.* **2007**, *107*, 1324.

- (2) Nunzi, J.-M. C. *R. Phys.* **2002**, *3*, 523.
- (3) Brabec, C. J.; Durrant, J. R. *MRS Bull.* **2008**, *33*, 670.
- (4) Brabec, C.; Dyakonov, V.; Scherf, U. *Organic Photovoltaics: Materials, Device Physics, and Manufacturing Technologies*; Wiley-VCH Verlag GmbH & Co. KGaA: Weinheim, 2008.
- (5) Coakley, K. M.; McGehee, M. D. *Chem. Mater.* **2004**, *16*, 4533.
- (6) Benanti, T. L.; Venkataraman, D. *Photosynth. Res.* **2006**, *87*, 63.
- (7) Dennler, G.; Scharber, M. C.; Brabec, C. J. *Adv. Mater.* **2009**, *21*, 1323.
- (8) Kim, K.; Liu, J.; Namboothiry, M. A. G.; Carroll, D. L. *Appl. Phys. Lett.* **2007**, *90*, 163511.
- (9) Kim, J. Y.; Kim, S. H.; Lee, H.-H.; Lee, K.; Ma, W.; Gong, X.; Heeger, A. J. *Adv. Mater.* **2006**, *18*, 572.
- (10) Kim, Y.; Choulis, S. A.; Nelson, J.; Bradley, D. D. C.; Cook, S.; Durrant, J. R. *Appl. Phys. Lett.* **2005**, *86*, 063502.
- (11) Erb, T.; Zhokhavets, U.; Gobsch, G.; Raleva, S.; Stuhn, B.; Schilinsky, P.; Waldauf, C.; Brabec, C. *Adv. Funct. Mater.* **2005**, *15*, 1193.
- (12) Liang, Y.; Xu, Z.; Xia, J.; Tsai, S.-T.; Wu, Y.; Li, G.; Ray, C.; Yu, L. *Adv. Mater.* **2010**, *22*, E135.
- (13) Mihailescu, V. D.; Xie, H. X.; de Boer, B.; Popescu, L. M.; Hummelen, J. C.; Blom, P. W. M.; Koster, L. J. A. *Appl. Phys. Lett.* **2006**, *89*, 021207.
- (14) Clarke, T. M.; Ballantyne, A. M.; Nelson, J.; Bradley, D. D. C.; Durrant, J. R. *Adv. Funct. Mater.* **2008**, *18*, 4029.
- (15) McNeill, C.; Watts, B.; Thomsen, L.; Belcher, W.; Kilcoyne, A.; Greenham, N.; Dastoor, P. C. *Small* **2006**, *2*, 1432.
- (16) Huang, Y.-C.; Liao, Y.-C.; Li, S.-S.; Wu, M.-C.; Chen, C.-W.; Su, W.-F. *Sol. Energy Mater. Sol. Cells* **2009**, *93*, 888.
- (17) Dante, M.; Peet, J.; Nguyen, T.-Q. *J. Phys. Chem. C* **2008**, *112*, 7241.
- (18) Wang, W. L.; Wu, H. B.; Yang, C. Y.; Luo, C.; Zhang, Y.; Chen, J. W.; Cao, Y. *Appl. Phys. Lett.* **2007**, *90*, 183512.
- (19) Ma, W.; Yang, C.; Gong, X.; Lee, K.; Heeger, A. J. *Adv. Funct. Mater.* **2005**, *15*, 1617.
- (20) Felicissimo, M. P.; Jarzab, D.; Gorgoi, M.; Forster, M.; Scherf, U.; Scharber, M. C.; Svensson, S.; Rudolf, P.; Loi, M. A. *J. Mater. Chem.* **2009**, *19*, 4899.
- (21) Barrau, S.; Andersson, V.; Zhang, F.; Masich, S.; Bijleveld, J.; Andersson, M. R.; Inganäs, O. *Macromolecules* **2009**, *42*, 4646.
- (22) Hoppe, H.; Glatzel, T.; Niggeman, M.; Schwinger, W.; Schaeffler, F.; Hinsch, A.; Lux-Steiner, M. Ch.; Saricic, N. S. *Thin Solid Films* **2006**, *511–512*, 587.
- (23) Drees, M.; Davis, R. M.; Heflin, J. R. *J. Appl. Phys.* **2005**, *97*, 036103.
- (24) Björström, C. M.; Nilsson, S.; Bernasik, A.; Budkowski, A.; Andersson, M.; Magnusson, K. O.; Moons, E. *Appl. Surf. Sci.* **2007**, *253*, 3906.
- (25) Chirvase, D.; Parisi, J.; Hummelen, J. C.; Dyakonov, V. *Nanotechnology* **2004**, *15*, 1317.
- (26) Reyes-Reyes, M.; Kim, K.; Dewald, J.; López-Sandoval, R.; Avadhanula, A.; Curran, S.; Carroll, D. L. *Org. Lett.* **2005**, *7*, 5749.
- (27) Waldauf, C.; Morana, M.; Denk, P.; Schilinsky, P.; Coakley, K.; Choulis, S. A.; Brabec, C. J. *Appl. Phys. Lett.* **2006**, *89*, 233517.
- (28) van Bavel, S. S.; Sourty, E.; de With, G.; Loos, J. *Nano Lett.* **2009**, *9*, 507.
- (29) Huang, J.-H.; Chien, F.-C.; Chen, P.; Ho, K.-C.; Chu, C.-W. *Anal. Chem.* **2010**, *82*, 1669.
- (30) Moon, J. S.; Lee, J. K.; Cho, S.; Byun, J.; Heeger, A. J. *Nano Lett.* **2009**, *9*, 230.
- (31) Wang, D. H.; Lee, H. K.; Choi, D. G.; Park, J. H.; Park, O. O. *Appl. Phys. Lett.* **2009**, *95*, 043505.
- (32) Chen, F.-C.; Lin, Y.-K.; Ko, C. J. *Appl. Phys. Lett.* **2008**, *92*, 023307.
- (33) Campoy-Quiles, M.; Ferenczi, T.; Agostinelli, T.; Etchegoin, P. G.; Kim, Y.; Anthopoulos, T. D.; Stavrinou, P. N.; Bradley, D. C.; Nelson, J. *Nat. Mater.* **2008**, *7*, 158.
- (34) Xu, Z.; Chen, L.-M.; Yang, G.; Huang, C.-H.; Hou, J.; Wu, Y.; Li, G.; Hsu, C.-S.; Yang, Y. *Adv. Funct. Mater.* **2009**, *19*, 1227.
- (35) Jo, J.; Na, S.-I.; Kim, S.-S.; Lee, T.-W.; Chung, Y.; Kang, S.-J.; Vak, D.; Kim, D.-Y. *Adv. Funct. Mater.* **2009**, *19*, 2398.
- (36) Yu, B.-Y.; Lin, W.-C.; Wang, W.-B.; Lida, S.-I.; Chen, S.-Z.; Liu, C.-Y.; Kuo, C.-H.; Lee, S.-H.; Kao, W.-L.; Yen, G.-J.; You, Y.-W.; Liu, C.-P.; Jou, J.-H.; Shyue, J.-J. *ACS Nano* **2010**, *4*, 833.
- (37) Parnell, A. J.; Dunbar, D. F.; Pearson, A. J.; Staniec, P. A.; Dennison, A. J. C.; Hamamatus, H.; Skoda, M. W. A.; Lidzey, D. G.; Jones, R. A. L. *Adv. Mater.* **2010**, *22*, 2444.
- (38) Germack, D. S.; Chan, C. K.; Kline, R. J.; Fischer, D. A.; Gundlach, D. J.; Toney, M. F.; Richter, L. J.; DeLongchamp, D. M. *Macromolecules* **2010**, *43*, 3828.
- (39) Wei, Q.; Nishizawa, T.; Tajima, K.; Hashimoto, K. *Adv. Mater.* **2008**, *20*, 2211.
- (40) Ohkita, H.; Cook, S.; Astuti, Y.; Duffy, W.; Tierney, S.; Zhang, W.; Heeney, M.; McCulloch, I.; Nelson, J.; Bradley, D. D. C.; Durrant, J. R. *J. Am. Chem. Soc.* **2008**, *130*, 3030.
- (41) Peet, J.; Salvatore, M. L.; Heeger, A. J.; Bazan, G. C. *Adv. Mater.* **2009**, *21*, 1521.
- (42) Chen, L.-M.; Hong, Z.; Li, G.; Yang, Y. *Adv. Mater.* **2009**, *21*, 1434.
- (43) Watts, B.; Thomsen, L.; Dastoor, P. C. *J. Electron Spectrosc. Relat. Phenom.* **2005**, *151*, 105.
- (44) Brown, P. J.; Thomas, D. S.; Köhler, A.; Wilson, J. S.; Kim, J.-S.; Ramsdale, C. M.; Sirringhaus, H.; Friend, R. H. *Phys. Rev. B* **2003**, *67*, 064203.
- (45) Guo, T.-F.; Wen, T.-C.; Pakhomov, G. L.; Chin, X.-G.; Liou, S.-H.; Yeh, P.-H.; Yang, C.-H. *Thin Solid Films* **2008**, *516*, 3138.
- (46) Zen, A.; Pflaum, J.; Hirschmann, S.; Zhuang, W.; Jaiser, F.; Asawapirom, U.; Rabe, J. P.; Scherf, U.; Neher, D. *Adv. Funct. Mater.* **2004**, *14*, 757.
- (47) Vanlaeke, P.; Swinnen, A.; Haeldermans, I.; Vanhoyland, G.; Aernouts, T.; Cheyns, D.; Deibel, C.; D'Haen, J.; Heremans, P.; Poortmans, J.; Manca, J. V. *Sol. Energy Mater. Sol. Cells* **2006**, *90*, 2150.
- (48) Stöhr, J. *NEXAFS Spectroscopy*; Springer Verlag: Heidelberg, 1992.
- (49) Ho, P. K.-H.; Chua, L.-L.; Dipankar, M.; Gao, X.; Qi, D.; Wee, A. T.-S.; Chang, J.-F.; Friend, R. H. *Adv. Mater.* **2007**, *19*, 215.
- (50) Germack, D. S.; Chan, C. K.; Hamadani, B. H.; Richter, L. J.; Fischer, D. A.; Gundlach, D. J.; DeLongchamp, D. M. *Appl. Phys. Lett.* **2009**, *94*, 233303.
- (51) McNeill, C. R.; Halls, J. J. M.; Wilson, R.; Whiting, G. L.; Berkebile, S.; Ramsey, M. G.; Friend, R. H.; Greenham, N. C. *Adv. Funct. Mater.* **2008**, *18*, 2309.
- (52) Prabhu, V. M.; Sambasivan, S.; Fischer, D.; Sundberg, L. K.; Allen, R. D. *Appl. Surf. Sci.* **2006**, *253*, 1010.
- (53) Aasmundtveit, K. E.; Samuelsen, E. J.; Pettersson, L. A. A.; Inganäs, O.; Johansson, T.; Feidenhans, R. *Synth. Met.* **1999**, *101*, 561.
- (54) Casu, M. B.; Cosseddu, P.; Batchelor, D.; Bonfiglio, A.; Umbach, E. *J. Chem. Phys.* **2008**, *128*, 014705.
- (55) Lang, U.; Müller, E.; Naujoks, N.; Dual, J. *Adv. Funct. Mater.* **2009**, *19*, 1215.
- (56) Nardes, A. M.; Kemerink, M.; Janssen, R. A. J.; Bastiaansen, J. A. M.; Kiggen, N. M. M.; Langeveld, B. M. W.; van Breemen, A. J. J. M.; de Kok, M. M. *Adv. Mater.* **2007**, *19*, 1196.
- (57) Wang, X.; Ederth, T.; Inganäs, O. *Langmuir* **2006**, *22*, 9287.
- (58) Yao, Y.; Hou, J.; Xu, Z.; Li, G.; Yang, Y. *Adv. Funct. Mater.* **2008**, *18*, 1783.
- (59) Li, G.; Shrotriya, V.; Huang, J.-S.; Yao, Y.; Moriarty, T.; Emery, K.; Yang, Y. *Nat. Mater.* **2005**, *4*, 864.
- (60) Mandoc, M. M.; Veurman, W.; Koster, L. J. A.; de Boer, B.; Blom, P. W. M. *Adv. Funct. Mater.* **2007**, *17*, 2167.
- (61) Mandoc, M. M.; Kooistra, F. B.; Hummelen, J. C.; de Boer, B.; Blom, P. W. M. *Appl. Phys. Lett.* **2007**, *91*, 263505.
- (62) Kline, R. J.; DeLongchamp, D. M.; Fischer, D. A.; Lin, E. K.; Richter, L. J.; Chabinyc, M. L.; Toney, M. F.; Heeney, M.; McCulloch, I. *Macromolecules* **2007**, *40*, 7960.
- (63) Kim, H. J.; Park, J. H.; Lee, H. H.; Lee, D. R.; Kim, J.-J. *Org. Electron.* **2009**, *10*, 1505.